Supporting Information

Shim et al. 10.1073/pnas.1115674109

SI Text

Derivation of Equation for Void-Volume Fraction, Eq. 2. To clarify the derivation of Eq. **2** in the main manuscript, we focus on the simplest case of the Buckliball with six voids (Fig. S1), although the argument is general and applicable to all other four configurations.

We start by deriving the relation between the angles (ϕ, θ and α) used in Eq. **2** of the main manuscript. We define ϕ as the angle between two vectors, which originate at the shell center and terminate at two neighboring vertices of a folded polyhedron (see the schematic diagram in Fig. S1*A*). Because the void's center in the expanded polyhedron (i.e., cuboctahedron for this specific case) is placed at the vertex locations of the folded polyhedron (i.e., octahedron for this specific case), ϕ also represents the angle relating the center-to-center distance between two adjacent circular voids in the expanded polyhedron. In addition, we define α as the angle that sets the narrowest width of the ligament (Fig. S1*B*), and θ as the angle that sets the diameter of the void (Fig. S1*B*). From geometry, we obtain

$$\theta = \phi - \alpha. \qquad \textbf{[S1]}$$

Secondly, we calculate the volume of the intact spherical shell:

$$V_{\text{shell}} = \frac{4}{3}\pi[R_o^3 - R_i^3], \qquad \textbf{[S2]}$$

where R_i and R_o denote the inner and outer radius of the shell, respectively.

We now need to calculate the volume of a single void on the spherical shell (Fig. S1*D*). Because each void is defined by a cone of opening angle θ and vertex located at the center of the sphere (Fig. S1*C*), its volume is given by

$$V_{\text{void}} = \frac{2}{3}\pi[R_o^3 - R_i^3]\left[1 - \cos\left(\frac{\theta}{2}\right)\right]. \qquad \textbf{[S3]}$$

Finally, combining Eqs. **S1**–**S3**, we obtain the following expression for the void-volume-fraction,

$$\psi = \frac{NV_{\text{void}}}{V_{\text{shell}}} = \frac{N}{2}\left[1 - \cos\left(\frac{\phi - \alpha}{2}\right)\right], \qquad \textbf{[S4]}$$

which corresponds to Eq. **2** in the main manuscript.

Phase Diagrams of Design Parameters $\langle\tau,\psi\rangle$. We present additional phase diagrams of design parameters for shells with 6, 30, and 60 holes, which are not included in Fig. 4 of the main manuscript because of the page limitation.

Because the experiments suggest that the narrowest cross-section of ligament in the expanded status of the spherical shells governs the on-sphere buckling behavior of the balls, by comparing the second moment of area along two axes (i.e., $I_{rr} \le I_{\theta\theta}$) we obtain a relation between the two design parameters $\langle\tau, \psi\rangle$ (Eqs. **2** and **3** in the main manuscript). The corresponding phase boundary is plotted as a marked line in Fig. S2. In addition, to assess our predictions, we perform a series of finite element simulations where we investigate the buckling of Buckliball characterized by different pairs of the design parameters $\langle\tau, \psi\rangle$. The phase diagrams for shells with 6, 30, and 60 holes are presented in Fig. S2. In these phase diagrams, regions where out-of-sphere (snap) buckling occurs are represented in white. In the shaded regions where encapsulation (i.e., on-sphere buckling) occurs, the color in the contour plots represents the associated critical buckling pressure for onset of on-sphere buckling (normalized by the Young's modulus E), given by the adjacent color bar. We find that the contour map boundary between the regions of on-sphere and out-of-sphere buckling is in good agreement with our analytical prediction based on the second moment of area of the narrowest cross-section of ligament.

Derivation of Equation for Pressure-Compression Relation, [4]. We proceed by presenting a detailed derivation of the scaling in **[4]** in the main manuscript (Eq. **[8]** in this document). We start by considering a single ligament and simplify its geometrical description using a curved column with uniform width ($w_e = R_i\alpha$) and effective column length ($L_e = \beta R_i\chi$) (Fig. S3). In the main manuscript, **[4]** can be obtained from the force equilibrium along the radial direction for the simplified curved column. To simplify the derivation, let's orient the column so that the radial direction at the center of its width coincides with the x axis of the Cartesian coordinate (see Fig. S3, *Right*). Introducing a spherical coordinate system ($r > 0,\ \theta \in [0, \pi],\ \varphi \in [0, 2\pi)$) so that $x = r\sin\theta\cos\varphi$, $y = r\sin\theta\sin\varphi$, and $z = r\cos\theta$, the component along the x direction (i.e., the radial direction) of the pressure p, denoted by F_x^p, can be obtained as

$$\begin{aligned} F_x^p &\approx \int_{\theta=\frac{\pi}{2}-\frac{\alpha}{2}}^{\theta=\frac{\pi}{2}+\frac{\alpha}{2}} \int_{\varphi=-\frac{\beta\chi}{2}}^{\varphi=\frac{\beta\chi}{2}} (p\sin\theta\cos\varphi) R_i^2 \sin\theta d\theta d\varphi \\ &\approx pR_i^2[\alpha + \sin\alpha]\sin\left(\frac{\beta\chi}{2}\right). \end{aligned} \qquad \textbf{[S5]}$$

Because the component along the x direction of the compressive force C, denoted by F_x^C, is given by

$$F_x^C = 2C\sin\left(\frac{\beta\chi}{2}\right), \qquad \textbf{[S6]}$$

force equilibrium in the x direction (i.e., $F_x^p = F_x^C$) yields

$$pR_i^2[\alpha + \sin\alpha] = 2C. \qquad \textbf{[S7]}$$

For large values of porosity $\alpha \to 0$, so that we can use the approximation $\sin\alpha \approx \alpha$, and Eq. **S7** reduces to

$$C \approx R_i^2\alpha p, \qquad \textbf{[S8]}$$

which corresponds to **[4]** in the main manuscript.

Postbuckling Analysis: Finite Element Simulations. Because the buckling analysis performed using Abaqus/Standar solver reveals that linear continuum elements lead to strong mesh-size dependent behavior, we built all the models using quadratic continuum elements (C3D10MH: a quadratic hybrid-continuum element with a 10-node modified tetrahedron having one additional variable relating to pressure) for both the thin membranes and the skeleton (thicker parts) of the shells.

Note that continuum elements are also used for the membrane, to resolve issues of compatibility between the quadratic continuum elements and linear shell elements for large-strain formulations. Although Abaqus/Standard provides various conventional thin shell element types, only few shell elements are suitable for large-strain analysis (1); these are linear thin shell

element (e.g., S3(R), S4(R), etc.) and quadratic thick shell elements (e.g., SC8(R), etc.), which are also called continuum shell elements. Both element types have a compatibility issue with quadratic continuum element types of *C3D10M(H)* and therefore we decide to use continuum elements for both the thin membranes and the thicker parts of the shells.

To perform the postbuckling analysis under volume-controlled conditions, the Buckliball was modeled as a spherical shell filled with fluid for which we used hydrostatic fluid elements (F3D3 with a mesh sweeping seed size of 1.25 mm). The fluid has been assumed to be compressible air having a density of 1.024 kg/m^3 at 20 °C and its volume has been progressively reduced during the simulations. Because Abaqus/Standard provides only linear hydrostatic fluid elements (element type *F3D3*), the mesh for the fluid elements was designed such that four fluid elements (i.e., four *F3D3* elements) are attached to a single face of the quadratic solid element (i.e., *C3D10MH*). In addition, implicit dynamic analysis were performed using Newmark algorithm with $\beta = 0.276$ and $\gamma = 0.550$ (such conditions are achieved by setting $\alpha = -0.05$, "*DYNAMIC, ALPHA = −0.05"). Note that this damping is purely numerical and is different from the material damping (2). The kinetic energy was monitored during simulations and observed to be less than 3.0% of the strain energy, ensuring quasi-static conditions.

A mesh sweeping seed size of 2.5 mm was chosen for the solid elements, resulting in hydrostatic fluid elements of size that is roughly half the size of the solid elements due to the above-mentioned mesh design procedure. For example, the model used for the postbuckling analysis of the Buckliball with membrane thickness $h = 0.5$ mm has 15,469 *C3D10MH* elements and 8,704 *F3D3* elements (Fig. S4*A*). Fig. S4*C* shows the results of the postbuckling analysis performed under volume-controlled conditions, which are presented in the main manuscript. The computational cost of the simulation was remarkably high; a single postbuckling analysis under volume control took 40 h using 48 central processing units. This extremely high computational cost for the volume-control simulations hindered further investigation on the effect of mesh size and numerical damping parameter.

For the sake of computational convenience, the accuracy of the mesh used in the volume-control simulations was ascertained performing several simulations under pressure-controlled conditions, whose computational cost is found to be less than one-fifth of that of the volume-controlled simulations. Therefore, models with sweeping mesh sizes of up to 1.0 mm were built and tested (see Fig. S4*B*).

For the static analysis under pressure-controlled conditions, a stabilized scheme using artificial damping was employed because the postbuckling behavior of the Buckliball covered by a thin membrane is characterized by two different types of sequential unstable buckling events (i.e., local snap-buckling events in the thin membranes followed by a global buckling mode of the skeleton). Note that the Abaqus/Standard solver provides an automatic stabilization with artificial damping; where viscous forces of the form $F_v = cM^*v$ are added to the global equilibrium equations; here, c is a damping factor, M^* is an artificial mass matrix calculated with unit density, and v is the nodal velocity vector. We choose an option where the damping factor c is determined in such a way that the dissipated energy for a given increment is 0.02% of the extrapolated strain energy, which is the default value by using the Abaqus keyword "*STATIC, STABILIZE = 0.0002". When we reduce the damping factor below 0.02%, the simulation stops before capturing the local snap-buckling of membranes. Thus, the damping factor of 0.02% is the smallest value with which the numerical simulations were still able to capture the correct postbuckling behavior. More details on this automatic stabilization scheme are presented in ref. 3.

Comparison of the results from the volume-controlled simulations (with mesh sweeping size of 2.5 mm shown in Fig. S4*C*) and pressure-controlled simulations (with mesh sweeping size of 1.0 mm shown in Fig. S4*D*) shows good agreement in terms of initial linear response and critical buckling pressure. These results confirm that the mesh size used in the volume-controlled simulations is fine enough to accurately predict the onset of buckling and postbucking behavior. Moreover, although the pressure-controlled simulations were unable to capture the experimentally observed softening that follows immediately after the onset of buckling, this feature was accurately predicted by the volume-controlled simulations.

Effect of Geometric Imperfections. We have performed an additional set of simulations to explore the imperfection sensitivity of buckling for the Buckliball, focusing on the Buckliball with 24 voids. The Buckliball had an inner radius $R_i = 22.5$ mm, shell thickness $t = 5$ mm, void-volume fraction $\psi = 58.7\%$, and the voids were not covered by a membrane. For this given Buckliball design, we introduced imperfections in the form of different void size and misplaced void location on the sphere when compared to their geometrically exact set by the underlying polyhedron. We explored the response of structures with stochastically displaced and sized voids of amplitude $a = 1\%t$, $5\%t$, $10\%t$, and $15\%t$ (i.e., $t = 5$ mm). Note that, for imperfections of magnitude larger than $15\%t$, the narrowest width of ligament vanishes so that the Buckliball loses structural integrity. Five configurations are generated and tested for each value of a, totaling 20 sets of simulations for both buckling and postbuckling analysis. The dependence of the critical buckling load as a function of a is presented in Fig. S5, showing that the critical pressure tends to decrease as the magnitude of imperfection increases. In addition, representative snapshots from the postbuckling analysis are shown in Fig. S6. For the cases with $a = 1\%t$ and $5\%t$, the pressure at the onset of buckling is found to be only marginally affected by imperfection (less than 1%) and all five configurations show a nearly perfect on-sphere buckling leading to the desired encapsulation behavior, and therefore only one representative snapshot is reported (Fig. S6 *A* and *B*). On the other hand, various postbuckled shapes are observed for the cases of $a = 10\%t$ and $15\%t$ and three representative snapshots are presented for each case (Fig. S6 *C* and *D*). As the magnitude of imperfection increases, the width of the ligaments of the Buckliball is strongly affected by the imperfections, so that the deformation tends to localize within the narrowest ligaments. For $a = 10\%t$, all five Buckliballs show the desired encapsulation postbuckling behavior, albeit with postbuckled shapes that can deviate from a sphere (Fig. S6*C*). Moreover, the pressure at buckling is reduced by roughly 7%. Finally, for $a = 15\%t$, the imperfection is found to strongly affect the response of the structures so that only one configuration out of five shows an encapsulation postbuckling behavior (Fig. S6*D*) and the critical pressure is now reduced by approximately 15%.

This additional set of simulations demonstrates that the encapsulation mechanism of the Buckliballs is robust and not affected by geometric imperfections up to $a = 10\%t$.

1. Abaqus (2008) *Abaqus Analysis User's Manual, Ver 6.8* (Dassault Systèmes Simulia Corp., Providence, RI), Sect 28.6.
2. Abaqus (2008) *Abaqus Theory Manual, Ver 6.8* (Dassault Systèmes Simulia Corp., Providence, RI), Sect 2.4.
3. Abaqus (2008) *Abaqus Analysis User's Manual, Ver 6.8* (Dassault Systèmes Simulia Corp., Providence, RI), Sect 7.1.

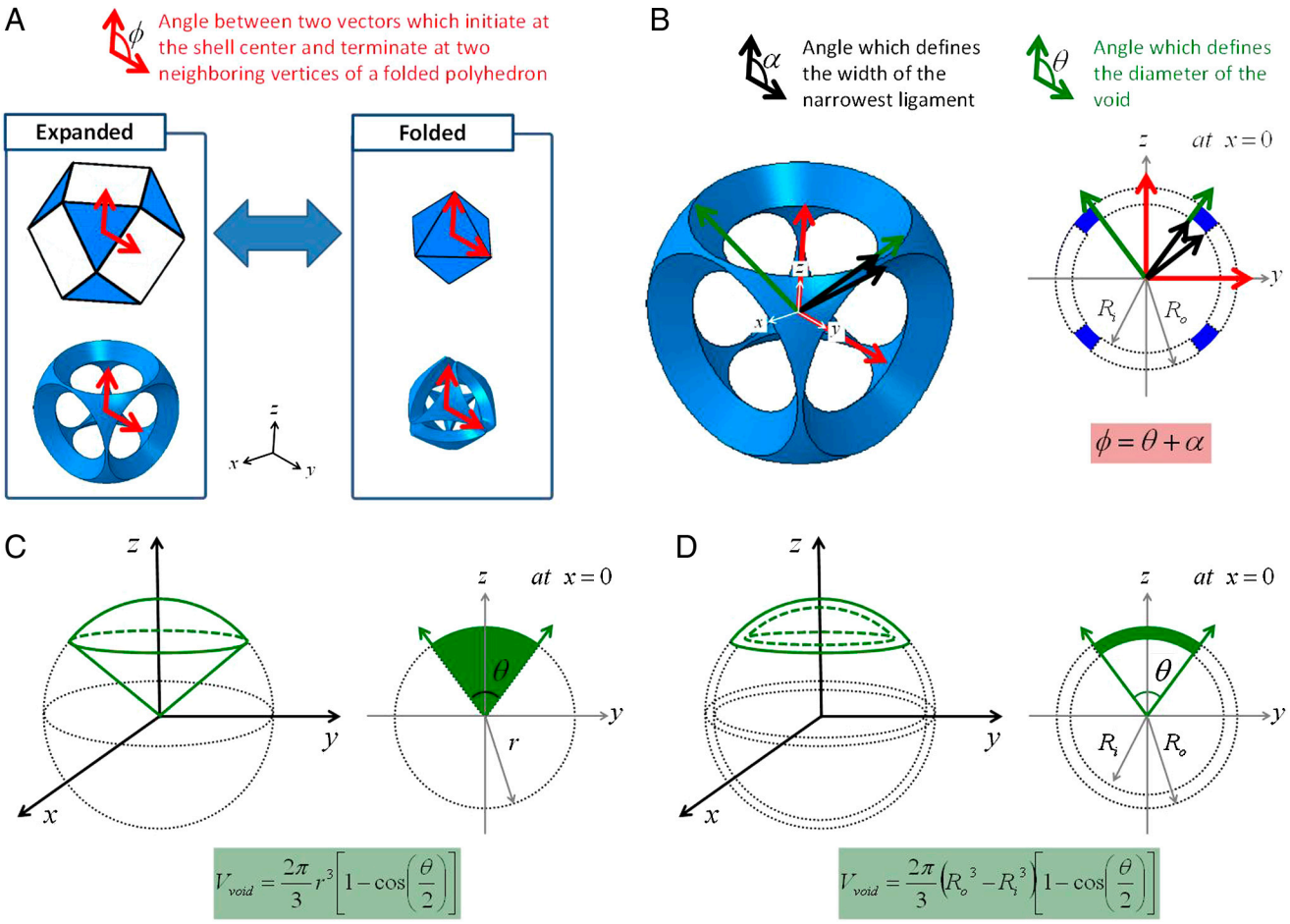

Fig. S1. Schematics illustrating (*A*) ϕ, (*B*) $\alpha$and θ, (*C*) a cone describing the hole on the spherical surface, and (*D*) the volume of each hole.

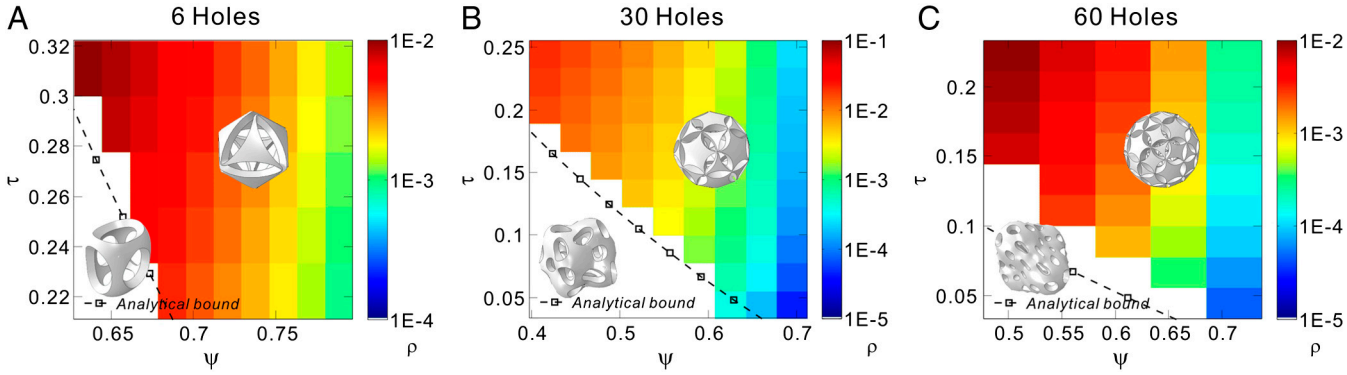

Fig. S2. Phase diagram of the two design parameters $\langle \tau, \psi \rangle$. The color-shaded region indicates on-sphere buckling and the white region represents the out-of-sphere buckling. The magnitude of the critical pressure for the onset of the on-sphere buckling is shown as a contour map with the adjacent color bar; (*A*) for 6 holes, (*B*) for 30 holes, and (*C*) for 60 holes.

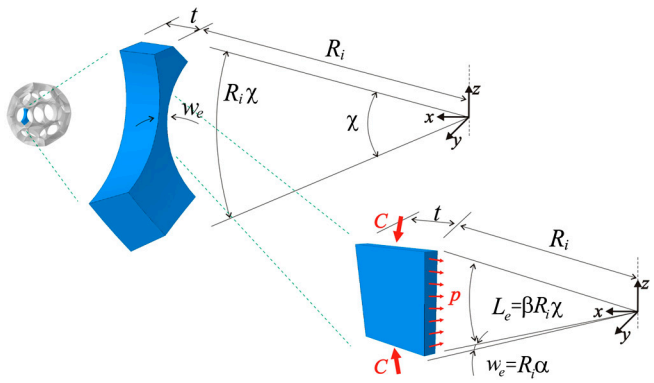

Fig. S3. Representative ligament extracted from the Buckliball and simplified curved column used in its buckling analysis.

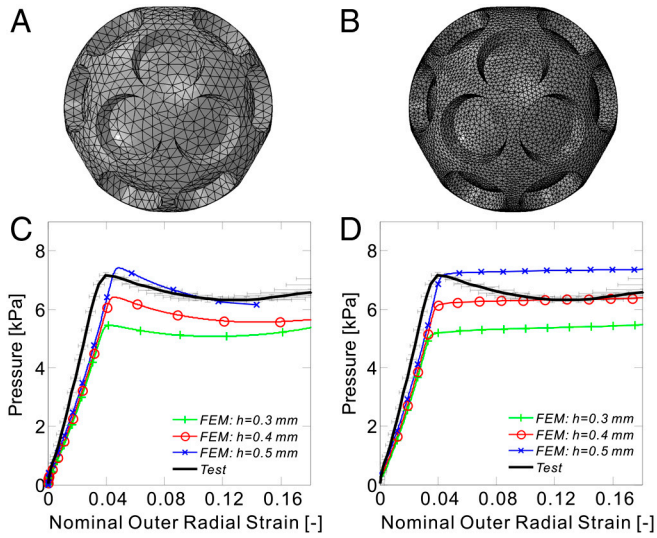

Fig. S4. (*A* and *B*) Meshed Buckliball with sweeping mesh size of (*A*) 2.5 mm and (*B*) 1.0 mm. (*C* and *D*) Dependence of the differential pressure of the ball on the nominal outer radial strain. Simulation results using finite element modeling (FEM), which are denoted by marked color lines, are obtained from (*C*) volume-controlled and (*D*) pressure-controlled conditions.

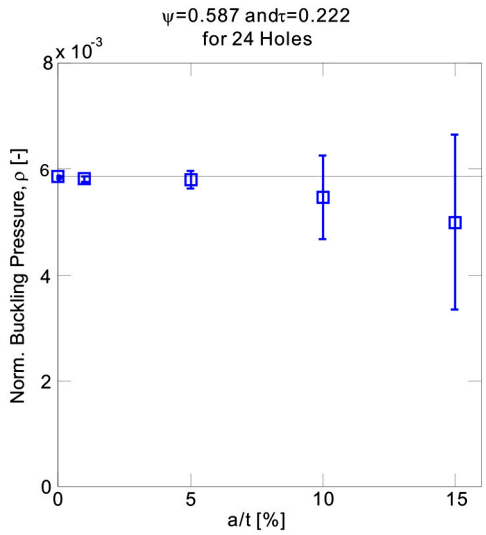

Fig. S5. Effect of imperfections on the normalized critical buckling pressure $\rho = p/E$. Blue square marks correspond to the mean value of five configurations and the size of error bar corresponds to the one-standard deviation. In addition, the black horizontal line represents the normalized critical buckling pressure for Buckliball without imperfections.

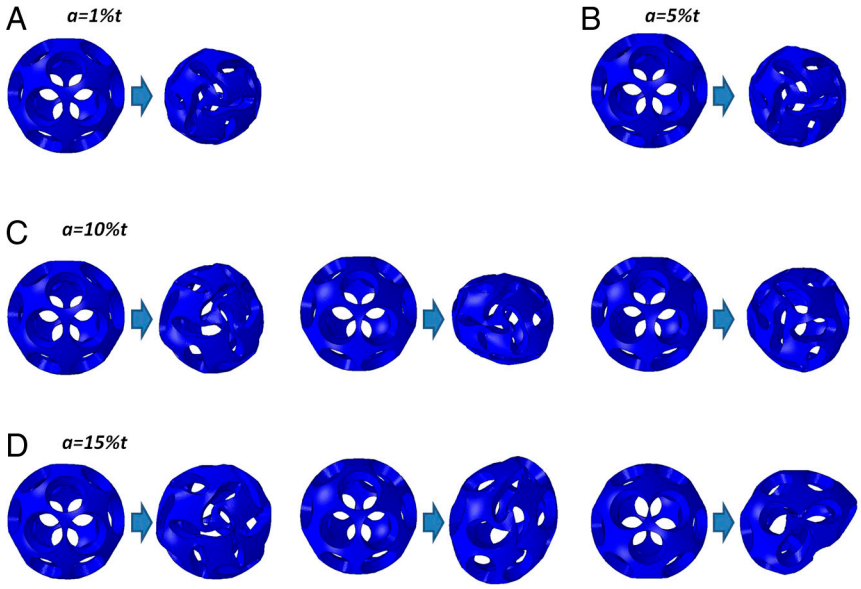

Fig. S6. Representative snapshots from the postbuckling analysis; (*A*) $a = 1\%t$ and (*B*) $a = 5\%t$. All five configurations remain spherical after buckling and show the encapsulation features. (*C*) For $a = 10\%t$, all five configurations show encapsulation features although after buckling their shapes significantly deviate from a sphere. (*D*) For $a = 15\%t$, only one configuration shows encapsulation features (*Left*), whereas all the others lead to irregularly collapsed shapes (*Center* and *Right*).